B. TECH. PROJECT REPORT

On

Estimation of Short Channel Effects in Shell-Doped Nanowire MOSFET

BY

Khushboo Ahuja
160002024

DISCIPLINE OF ELECTRICAL ENGINEERING
INDIAN INSTITUTE OF TECHNOLOGY INDORE

DECEMBER 2019

Estimation of Short Channel Effects in Shell-Doped Nanowire MOSFET

A PROJECT REPORT

Submitted in partial fulfillment of the
requirements for the award of the degree
of
BACHELOR OF TECHNOLOGY
in
ELECTRICAL ENGINEERING

Submitted by:
Khushboo Ahuja

Guided by:
Prof. Abhinav Kranti
Discipline of Electrical Engineering
Indian Institute of Technology Indore

INDIAN INSTITUTE OF TECHNOLOGY INDORE
DECEMBER 2019

CANDIDATE'S DECLARATION

We hereby declare that the project entitled **"Estimation of Short Channel Effects in Shell-Doped Nanowire MOSFET"** submitted in partial fulfillment for the award of the degree of Bachelor of Technology in 'Electrical Engineering' completed under the supervision of **Dr. Abhinav Kranti,** Professor, Discipline of Electrical Engineering, IIT Indore is an authentic work.

Further, I declare that I have not submitted this work for the award of any other degree elsewhere.

Khushboo Ahuja

CERTIFICATE by BTP Guide

It is certified that the above statement made by the student is correct to the best of my knowledge.

Dr. Abhinav Kranti

Professor

Discipline of Electrical Engineering

IIT Indore

Preface

This report on "**Estimation of Short Channel Effects in Shell-Doped Nanowire MOSFET**" is prepared under the guidance of **Dr. Abhinav Kranti,** Professor, Discipline of Electrical Engineering, IIT Indore.

(I have given a detailed description of the derivation of an analytical model for a newly introduced unconventional transistor, shell-doped cylindrical nanowire junctionless MOSFET through this report. The derived model is verified using preliminary tests and the results obtained from the model are included in the report)

Khushboo Ahuja
B.Tech. IV Year
Discipline of Electrical Engineering
IIT Indore

Acknowledgements

I would like to express my sincere gratitude to my B.Tech. project supervisor, Prof. Abhinav Kranti, for his valuable guidance and support throughout the course of this project.

I would also like to thank Ms. Nivedita Jaiswal, Ph.D. scholar at Low Power Nanoelectronics Research Lab, Discipline of Electrical Engineering, for her constant help and motivation.

I would like to acknowledge IIT Indore for providing all the necessary equipments and infrastructure for carrying out this B.Tech. Project.

Khushboo Ahuja
B.Tech. IV Year
Discipline of Electrical Engineering
IIT Indore

Abstract

In this project, an analytical model is derived for a recently introduced unconventional transistor, cylindrical nanowire junctionless metal oxide semiconductor field effect transistor (CNW JL MOSFET). CNW JL MOSFET has emerged as a promising device which can overcome the challenges of downscaling associated with the conventional MOSFETs and junctionless transistors. Thus, the derived analytical model will help in understanding and optimizing the properties in the subthreshold regime of the device.

The uniqueness of this work lies in introducing a new potential approximation function for deriving the potential model of the device as the existing method of parabolic approximation failed to give physically acceptable model for CNW JL MOSFET. The preliminary verification of the derived model was done by using some key indicators obtained during model development. Finally, the results obtained from the derived potential model were presented and analyzed.

Table of Contents

Candidate's Declaration | Certificate by BTP Guide II

Preface III

Acknowledgements IV

Abstract V

List of Figures VIII

Chapter 1 Introduction 1

1.1 Motivation 1

1.2 Metal Oxide Semiconductor Field Effect Transistor 2

1.2.1 Overview 2

1.2.2 Challenges 3

1.3 Junctionless Field Effect Transistor 3

1.3.1 Overview 3

1.3.2 Challenges 4

1.4 Shell Doped Junctionless Transistor 4

1.4.1 Overview 4

1.4.2 Structure 5

1.4.3 Cylindrical Topology 5

Chapter 2 Model Development 7

2.1 Literature Survey 7

2.2 Limitation of the Parabolic Approximation function 8

2.3 Model Development for Shell-Doped CNW JL MOSFET 8

2.3.1 Modeling Considerations 8

2.3.2 Poisson's Equations 10

2.3.3 New Potential Function 10

2.3.4 Boundary Conditions along radial direction 11
2.3.5 Conversion to 1-D equation in central potential 12
2.3.5.1 Central Potential in Gated Region 12
2.3.5.2 Central Potential in Extension Regions 13
2.3.6 Boundary conditions in axial direction 14
Chapter 3 Results and Preliminary Analysis 17
3.1 Key Indicators 17
3.2 Parabolic Approximation Function 17
3.3 New Approximation Function 18
3.4 Validity of New Function over Parabolic Function 19
3.5 Modeled Results 20
Chapter 4 Conclusion and Scope for Future Work 23
4.1 Conclusion 23
4.2 Scope for Future Work 23
References 25

List of Figures

Figure 1.1: Schematic diagram of n-channel MOSFET where L_g denotes the gate length.

Figure 1.2: Schematic diagram of n-channel JFET where L_g denotes gate length.

Figure 1.3: Shell-doped transistor architecture as a combination of conventional MOSFET and Junctionless Field Effect Transistor (JFET).

Figure 1.4: Schematic of shell-doped cylindrical nanowire junctionless MOSFET

Figure 2.1: Circular cross-sectional view of shell-doped CNW JL MOSFET.

Figure 2.2: Longitudinal cross-sectional view of shell-doped CNW JL MOSFET.

Figure 3.1: Long channel potential (V_L) for different values of R_{Core} for derived models.

Figure 3.2: Ratio of equivalent doping (N_0) and shell doping (N_d) for different values of R_{Core} for derived models.

Figure 3.3: Variation of potential along radial direction at $z=L_g/2$ for different values of R_{Core}.

Figure 3.4: Variation of central potential ($\phi_0(z)$) along axial direction for different values of R_{Core}.

Figure 3.5: Comparison of channel potential of shell-doped DG JL MOSFET and developed shell-doped CNW JL MOSFET.

Chapter 1

INTRODUCTION

1.1 Motivation

Transistors are the key components in all modern electronics. The most widely used transistor is the metal–oxide–semiconductor field-effect transistor (MOSFET) with applications ranging from computers and electronics to communication technology [1]. Over several decades, the semiconductor industry has continuously scaled the transistor's dimensions to fit more and more transistors on a single chip, with the smallest transistor reaching a size of around 10 nm [2]. However, continuous downscaling increases short channel effects (SCEs) and leads to poor subthreshold characteristics in a conventional MOSFET [2], [3]. Multi-gate device topologies like double gate, tri-gate and gate-all-around MOSFETs have continuously been introduced to offer better control over SCEs while keeping up the pace with Moore's law scaling projections [2], [3]. Also, newer devices (e.g., junctionless transistors [3], [4]) have been widely investigated to obtain better performance than conventional MOSFETs. One such recent introduction in the list of unconventional MOSFETs is shell-doped nanowire MOSFET [6], [7].

A shell-doped cylindrical nanowire junctionless (CNW JL) transistor has two different doping regions [8]. The outer shell is heavily doped and the inner core is very lightly doped or undoped. The shell-doped nanowire junctionless (JL) MOSFET has shown significant improvement over the conventional nanowire JL MOSFET in achieving better SCEs [8]. The device has also shown potential of overcoming problems like band-to-band tunneling (BTBT) and random dopant fluctuations (RDFs) which are prevalent in a conventional JL MOSFET [8]-[10]. Thus, the project aims to develop an analytical model to estimate the channel potential in the subthreshold region of the device and analyze the SCEs using this channel potential expression. This work will help in understanding the device physics and performance, and in optimizing the device parameters for subthreshold logic applications.

1.2 Metal Oxide Semiconductor Field Effect Transistor

1.2.1 Overview

MOSFET is a core of the integrated circuit and the most common transistor in the semiconductor industry. It has applications in analog, digital and memory circuits [1]. Figure 1.1 shows an n-channel MOSFET with source, drain, gate, and body terminals. There are four terminals in a MOSFET- source (S), drain (D), gate (G), and body (B) terminals. A dielectric layer of oxide insulates the channel from the gate terminal. The voltage applied on the gate terminal electronically controls the formation of channel between source and drain regions. When suitable drain to source bias is applied on the MOSFET terminals, the flow of charge carriers takes place in the channel from source to drain [1], [11].

MOSFET operates on the concept of metal-oxide-semiconductor (MOS) Capacitor. The conduction and valence bands' positions (relative to the Fermi level) at the semiconductor-oxide interface depends on the gate terminal voltage of the device, also referred to as the MOS capacitor voltage. By applying a proper MOS capacitor voltage, the semiconductor surface can be inverted from p-type to n-type in an n-channel MOSFET or from n-type to p-type in a p-channel MOSFET [11]. The creation of the thin inversion charge density near the semiconductor surface is the basis of the operation and characteristics of the MOSFET [11].

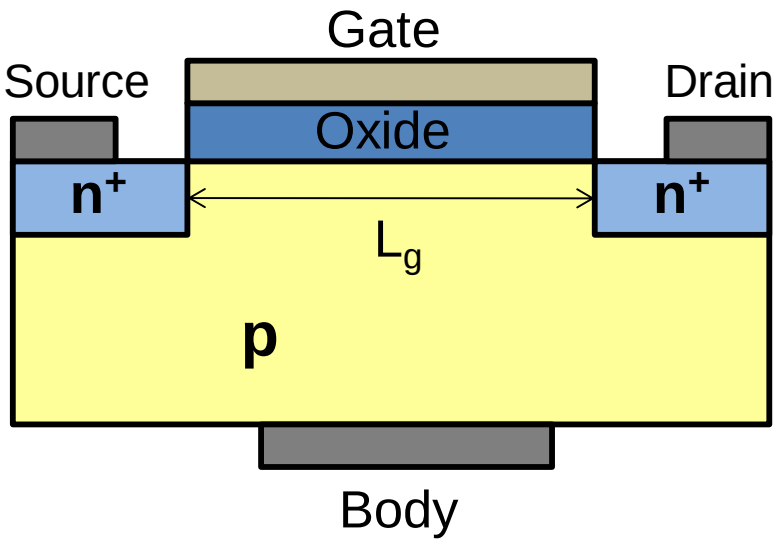

Figure 1.1 Schematic diagram of n-channel MOSFET where L_g denotes the gate length

1.2.2 Challenges

When the channel length of a MOSFET approaches the widths of source and drain depletion layers, several SCEs like drain induced barrier lowering (DIBL), degradation in subthreshold swing, velocity saturation, surface scattering etc. come into effect [1], [11]. With the reduction in the channel length of the device, the potential, which is one-dimensional for a long channel device, becomes two-dimensional in nature. This results in the reduction of the MOSFET's threshold voltage and it also leads to its dependence on the biasing voltages and gate length. The punch through effect also comes into picture which leads to failure of the current saturation [11]. All these short channel effects, therefore, put a limitation on the downscaling of the device.

1.3 Junctionless Field Effect Transistor

1.3.1 Overview

The junctionless transistor was first introduced in 2010 by J.P. Colinge's group [5]. The conventional MOS devices known were based on pn junctions. These pn junctions are formed by adding dopant atoms into the base semiconductor material. As the process of downscaling continues to nanometre regime in modern devices, the distance between junctions has dropped below 10 nm [2]. As a result, high doping concentration gradients become necessary for the fabrication of modern devices with junctions. The statistical nature of the distribution of the dopant atoms and the laws of diffusion pose difficult fabrication challenges with these ultra-sharp doping gradients. Therefore, the introduction of the junctionless transistors, with no junctions, helps in overcoming this fabrication difficulty [5].

Figure 1.2 shows the structure of an n-channel junctionless field effect transistor (JFET). Junctionless Field Transistor (JFET) is a heavily doped semiconductor device with uniform doping of 5×10^{18} to 10^{19} cm^{-3}. The channel region concentration is controlled by the gate terminal which has a high work-function material [5]. The device can be switched off for zero bias with a suitable gate work-function. A JFET has full CMOS functionality [5]. As compared to the traditional MOSFET, the device shows better subthreshold characteristics with near-ideal

subthreshold slope, low leakage currents and less gate voltage-induced degradation of mobility [4],[5].

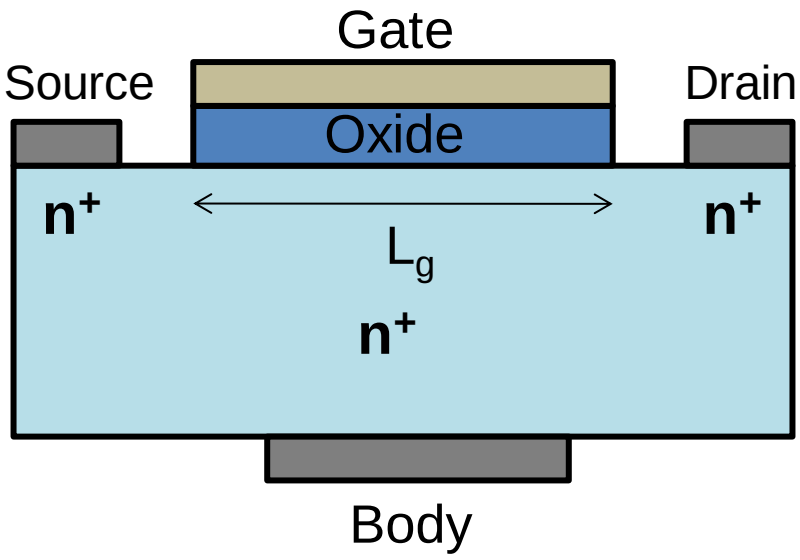

Figure 1.2 Schematic diagram of n-channel JFET where L_g denotes gate length

1.3.2 Challenges

Due to the heavy doping in junctionless transistor, the JL device poses problems like RDFs which leads to variation in device characteristics [9]. This high doping also leads to off-state BTBT of carriers in the device, causing considerable rise in the leakage current [10].

1.4 Shell Doped Junctionless Transistor

1.4.1 Overview

Recently, a junctionless structure with shell-doping profile has been introduced [6],[7] that has shown significant improvement over the conventional junctionless FET in terms of SCEs, RDF and BTBT while retaining the simplicity of fabrication [8]. The device is, therefore, seen as a promising device which can offer a whole new scope of downscaling and process optimization.

1.4.2 Structure

The shell doped junctionless MOSFET has a state-of-an transistor architecture and it can be seen as a structure formed by the combination of a conventional MOSFET and a junctionless field effect transistor [7]. The device, therefore, possess a complicated structure with different doping regions.

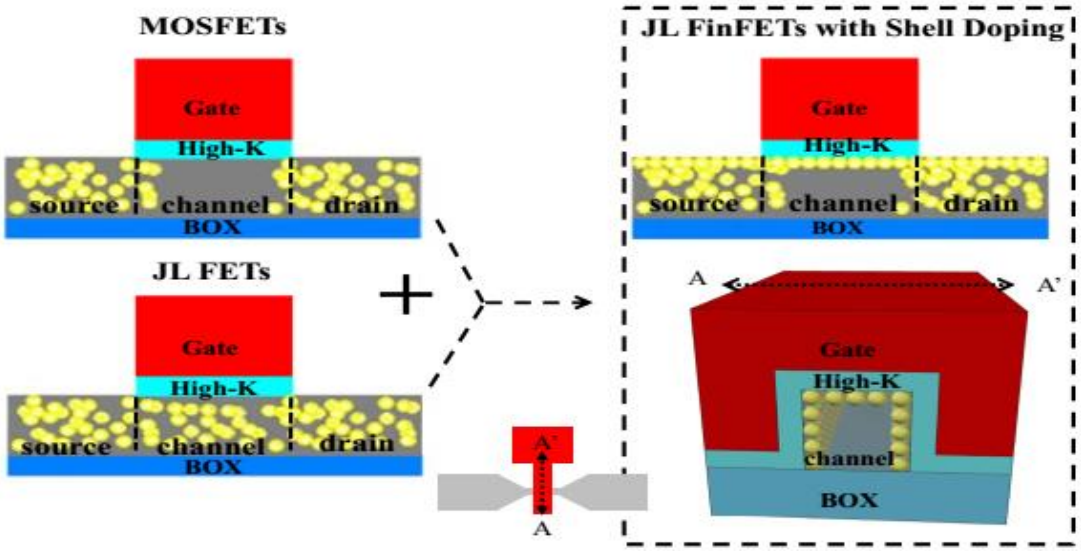

Figure 1.3 Shell-doped transistor architecture as a combination of conventional MOSFET and Junctionless Field Effect Transistor (JFET) [7]

1.4.3 Cylindrical Topology

The cylindrical topology offers many advantages over the conventional planar structure of the device. The gate-all-around structure offers better electrostatic control over the channel which leads to suppressed SCEs and improved subthreshold characteristics in the device [3]. Thus, the project aims to develop an analytical model for shell-doped cylindrical nanowire junctionless (CNW JL) MOSFET in subthreshold region of operation to better understand the working of transistor and help in optimization.

A shell-doped CNW JL transistor has two different doping regions. The outer shell is heavily doped and the inner core is very lightly doped or undoped. Figure 1.4 shows the schematic of a shell doped CNW JL transistor.

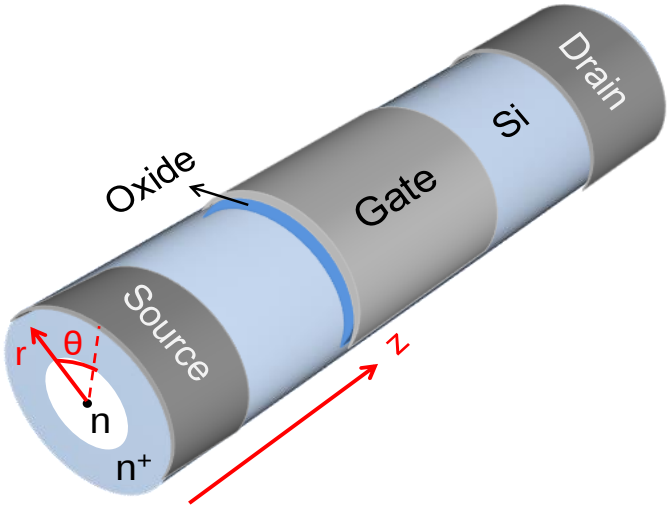

Figure 1.4 Schematic of shell-doped cylindrical nanowire junctionless MOSFET

Chapter 2

MODEL DEVELOPMENT

2.1 Literature Survey

The existing work in the literature related to modeling of different devices was studied for conventional and junctionless MOSFETs (both planar and cylindrical structures) [12]-[15]. There are different methods by which analytical models for these devices are developed through the solution of Poisson's equation. All methods were analyzed to finalize the approach for model development for the shell-doped CNW JL MOSFET. The modeling in the subthreshold region involves solving Poisson's equation to obtain the channel potential ($\phi(r,z)$) expression.

Two of the major approaches followed for solving the Poisson's equation are:

(i) Parabolic approximation of potential [13] and

(ii) Solution involving decomposition into long channel and short channel potentials [14].

Salient features of both are outlined as follows:

1. The first method assumes the potential to be a parabolic function along the radial direction having arbitrary coefficients a(z), b(z) and c(z) as functions of axial direction (z) [13], as follows:

$$\phi(r,z) = a(z)r^2 + b(z)r + c(z) \quad (1)$$

2. The second method of directly solving the Poisson's equation involves expressing the 2-D potential expression as a sum of long channel (V(r)) and short channel (U(r,z)) potentials [14] as follows:

$$\phi(r,z) = U(r,z) + V(r) \quad (2)$$

Both the approaches have shown good results for conventional planar as well as cylindrical MOSFETs [12]-[15]. However, the decomposition method requires a series solution which is often approximated through first order terms [14] whereas the parabolic method is relatively

simpler and results in an expression for natural length [15]. This natural length characterizes short channel effects and acts as a crucial indicator for preliminary validation of the developed analytical model. Thus, the parabolic approximation method was finalized for solving the Poisson's equation in CNW JL MOSFET to develop the analytical model for the device.

2.2 Limitations of the parabolic approximation method

The parabolic approximation method involves assumption of a parabolic function for the core and shell potential along radial direction as follows:

$$\phi_{Shell,m}(r,z) = a_{0m}(z) + a_{1m}(z)r + a_{2m}(z)r^2 \tag{3}$$

$$\phi_{Core,m}(r,z) = b_{0m}(z) + b_{1m}(z)r + b_{2m}(z)r^2 \tag{4}$$

Here $\phi_{Shell}(r,z)$ is the potential in the shell region, $\phi_{core}(r,z)$ is the potential in the core region, a_{0m}, a_{1m}, a_{2m}, b_{0m}, b_{1m}, b_{2m} are the arbitrary coefficients to be obtained using the appropriate boundary conditions along the radial direction.

When (3) and (4) were used to solve the Poisson's equations in CNW JL MOSFET, the derived model did not pass the preliminary tests for the validation of the model. Thus, the widely accepted parabolic approximation method showed limitations and thus, could not be used to derive the analytical model in this case. This is analyzed in detail in section 3.2.

2.3 Model Development for Shell-doped CNW JL MOSFET

2.3.1 Modeling Considerations

Figure 2.1 and 2.2 show the circular and longitudinal cross-sectional view of the device respectively. The central region with radius R_{Core} is lightly doped while the shell of thickness (R_{Si}-R_{Core}) is heavily doped. L_g and T_{ox} indicate gate length and gate oxide thickness, respectively. Regions 1 and 3 in figure 2.2 denote the extensions on the source and drain side

respectively, where the gate electric field has influence beyond the gated region [16],[17]. L_{Sext} and L_{Dext} denote the lengths of these extensions on source and drain side respectively. Due to the gradient in the doping in the radial direction, the diffusion of the carriers also takes place in this direction [8]. The device potential $\phi(r,z,\theta)$ is 3-D in nature but the device is symmetric in the θ direction as shown in figure 2.1. This makes the analytical modeling of the device 2-D in nature.

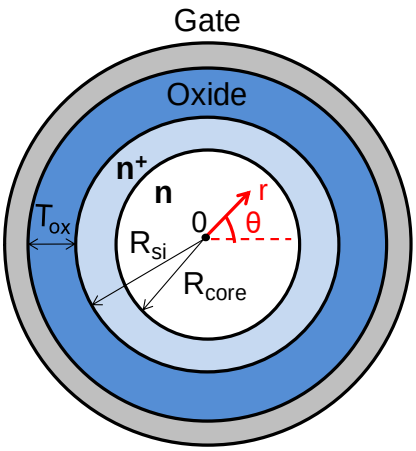

Figure 2.1 Circular cross-sectional view of shell-doped CNW JL MOSFET

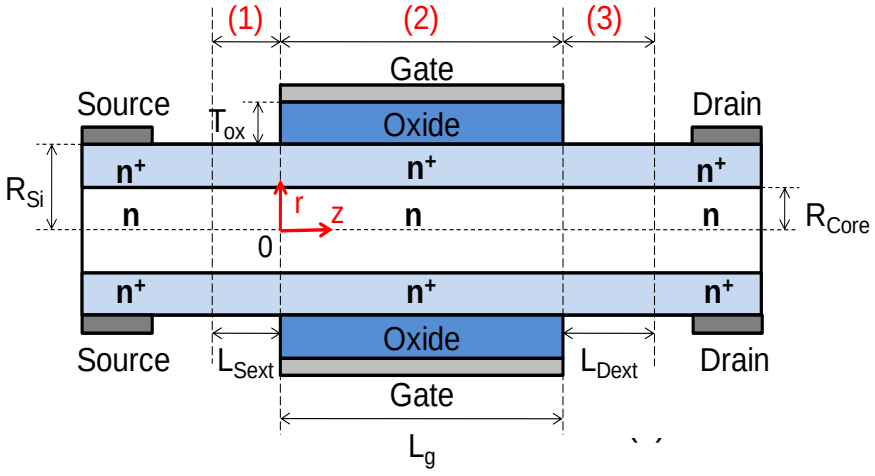

Figure 2.2 Longitudinal cross-sectional view of shell-doped CNW JL MOSFET

2.3.1 Poisson's Equations

The development of the analytical model in the subthreshold regime involves solving of the Poisson's equation to obtain the 2-D potential expression ϕ(r,z). The Poisson's equations [13], [14] in the shell and core regions of the shell-doped CNW JL MOSFET are given as:

A.) Shell:

$$\frac{\partial^2 \phi_{Shell,m}(r,z)}{\partial r^2} + \frac{1}{r}\frac{\partial \phi_{Shell,m}(r,z)}{\partial r} + \frac{\partial^2 \phi_{Shell,m}(r,z)}{\partial z^2} = \frac{-qN_D}{\varepsilon_{si}} \tag{5}$$

B.) Core:

$$\frac{\partial^2 \phi_{Core,m}(r,z)}{\partial r^2} + \frac{1}{r}\frac{\partial \phi_{Core,m}(r,z)}{\partial r} + \frac{\partial^2 \phi_{Core,m}(r,z)}{\partial z^2} = \frac{-qN_C}{\varepsilon_{si}}\left(1 - \frac{n_{i,Core}}{N_C}\exp\left(\frac{\phi_{Core,m}(r,z) - V_f(z)}{V_T}\right)\right) \tag{6}$$

Here $\phi_{Shell}(r,z)$ is the 2-D potential in shell region, $\phi_{core}(r,z)$ is the 2-D potential in the core region, m is 1, 2 or 3 depending on the region of the device as shown in figure 2.2, q is the charge of an electron, ε_{si} is the silicon permittivity, $n_{i,Core}$ is the intrinsic carrier concentration of core-Si, V_T is the thermal voltage (=KT/q) where K is the Boltzman's constant and T is the temperature, $V_f(z)$ is electron quasi-fermi potential.

2.3.2 New Potential Function

As the well established parabolic potential approximation [13] failed to give results for shell-doped CNW JL MOSFET, a new function was considered for potential expression along the radial direction in shell and core regions of the device:

$$\phi_{Shell,m}(r,z) = a_{0m}(z) + a_{1m}(z)\ln(r) + a_{2m}(z)r^2 \tag{7}$$

$$\phi_{Core,m}(r,z) = b_{0m}(z) + b_{1m}(z)\ln(r) + b_{2m}(z)r^2 \tag{8}$$

Here a_{0m}, a_{1m}, a_{2m}, b_{0m}, b_{1m}, b_{2m} are the arbitrary coefficients to be obtained using the appropriate boundary conditions along the radial direction in regions 1, 2 and 3.

2.3.3 Boundary Conditions along radial direction

The following boundary conditions are applied suitably to the above potential expressions to obtain the values of arbitrary coefficients in (7) and (8):

1.) Potential on the surface ($r=R_{Si}$) and at the centre ($r=0$) in regions 1, 2 and 3:

$$\phi_{Shell,m}(r=R_{Si},z)=\phi_{s,m}(z)$$
$$\phi_{Core,m}(r=0,z)=\phi_{0,m}(z) \quad (9)$$

where m=1, 2 or 3 depending on the region as shown in figure 2.2.

2.) Electric field at centre ($r=0$) in all the 3 regions: As the device is symmetric along the axis,

$$\left.\frac{\partial\phi_{Core,m}(r,z)}{\partial r}\right|_{r=0}=0 \quad (10)$$

where m=1, 2 or 3 depending on the region as shown in figure 2.2.

3.) Electric field at the surface ($r=R_{Si}$) in regions 1 and 3: We neglect the outer fringing effect [18],[19], and thus, it can be approximated as 0.

$$\left.\frac{\partial\phi_{Shell,n}(r,z)}{\partial r}\right|_{r=R_{Si}}\approx 0 \quad (11)$$

Here, n is 1 or 3 depending on the device region.

4.) Electric field at the surface ($r=R_{Si}$) in region 2 [20]-[23]:

$$\left.\frac{\partial\phi_{Shell,2}(r,z)}{\partial r}\right|_{r=R_{Si}}=g\left(V_{gs}^{'}-\phi_{s,2}(z)\right) \quad (12)$$

where $g=\varepsilon_{ox}/\varepsilon_{si}\,R_{si}\ln(1+T_{ox}/R_{Si})$, $V'_{gs}=V_{gs}-V_{fb}$ where ε_{ox} and T_{ox} are oxide permittivity and thickness respectively, V_{gs} is the gate bias with respect to source and V_{fb} is the flatband potential with respect to intrinsic Si.

5.) Continuity of the vertical electric field and potential in regions 1, 2 and 3 at $r=R_{Core}$:

$$\phi_{Shell,m}(r=R_{Core},z)=\phi_{Core,m}(r=R_{Core},z)$$

$$\left.\frac{\partial\phi_{Shell,m}(r,z)}{\partial r}\right|_{r=R_{Core}}=\left.\frac{\partial\phi_{Core,m}(r,z)}{\partial r}\right|_{r=R_{Core}} \quad (13)$$

where m=1, 2 or 3 depending on the region of the device.

2.3.4 Conversion to 1-D equation in central potential

In the subthreshold regime, the potential along r=0 ($\phi_{0,m}(z)$) has the lowest value in the device and thus, it is the main determinant of the subthreshold characteristics of the device [12]. Therefore, to obtain a simplified analytical model for the analysis of subthreshold properties of the device, the above 2-D equations are converted into 1-D equation in terms of central potential $\phi_{0,m}(z)$. This process also has the added advantage of providing some crucial key indicators which can be used for the preliminary verification of the derived model. This is discussed in detail in chapter 3.

2.3.4.1 Central Potential in Gated Region

The arbitrary coefficients in (7) and (8) are obtained for the gated region using appropriate boundary conditions from (9) to (13) in the radial direction.

The potential expressions in shell and core part of the gated region are obtained as:

$$\phi_{Shell,2}(r,z)=\phi_{s,2}(z)+\left[\frac{q(N_D-N_C)}{2\varepsilon_{Si}}R_{Core}^2\right]\ln\left(\frac{r}{R_{Si}}\right)+\left[\frac{g(V_{gs}^{'}-\phi_{s,2}(z))}{2R_{Si}}-\frac{q(N_D-N_C)}{4\varepsilon_{Si}}\frac{R_{Core}^2}{R_{Si}^2}\right](r^2-R_{Si}^2) \quad (14)$$

$$\phi_{Core,2}(r,z)=\phi_{0,2}(z)+\left[\frac{g(V_{gs}^{'}-\phi_{s,2}(z))}{2R_{Si}}-\frac{q(N_D-N_C)}{4\varepsilon_{Si}}\left(\frac{R_{Core}^2}{R_{Si}^2}-1\right)\right]r^2 \quad (15)$$

The gated region (region 1) is fully depleted of mobile carriers in the subthreshold regime ($n_{i,Core}$=0) and thus, (6) will change accordingly. Poisson's equations (5) and (6) are solved simultaneously at r=R_{Core} to obtain relation between $\phi_{0,2}(z)$ and $\phi_{s,2}(z)$:

$$\phi_{s,2}(z)=\frac{\phi_{0,2}(z)+\frac{g\,R_{Si}V_{gs}^{'}}{2}+\frac{q(N_D-N_C)R_{Core}^2}{2\varepsilon_{Si}}\ln\left(\frac{R_{Si}}{R_{Core}}\right)}{1+(g\,R_{Si}/2)} \tag{16}$$

Using (14)-(16) in equation (6) at r=0 gives 1-D differential equation in $\phi_{0,2}(z)$:

$$\frac{d^2\phi_{0,2}(z)}{dz^2}=\frac{\phi_{0,2}(z)-V_L}{\lambda^2} \tag{17}$$

Here, $V_L=V_{gs}^{'}+\frac{q\lambda^2}{\varepsilon_{si}}\left[N_D-\frac{(N_D-N_C)R_{Core}^2}{2\lambda^2}\left(\frac{2\lambda^2}{R_{Si}^2}+\ln\left(\frac{R_{Si}}{R_{Core}}\right)\right)\right]$ and $\lambda=\sqrt{(2R_{Si}+gR_{Si}^2)/4g}$ are the expressions of long channel potential and natural length respectively. These expressions act as crucial key indicators which can be used for primary verification of the derived model.

The general solution of (17) is given as:

$$\phi_{0,2}(z)=A_1\exp(z/\lambda)+A_2\exp(-z/\lambda)+V_L \tag{18}$$

where A_1 and A_2 are arbitrary coefficients to be obtained using boundary conditions in the axial direction.

2.3.4.2 Central Potential in Extension Regions

On applying the appropriate boundary conditions from (9) to (13), (7) and (8) give the potential expressions in the shell and core part of the extension regions 1 and 3:

$$\phi_{Shell,n}(r,z)=\phi_{s,n}(z)+\left[\frac{\phi_{s,n}(z)-\phi_{0,n}(z)}{\ln(R_{Si}/R_{Core})}\right]\ln\left(\frac{r}{R_{Si}}\right)+\left[\frac{\phi_{0,n}(z)-\phi_{s,n}(z)}{R_{Si}^2\ln(R_{Si}^2/R_{Core}^2)}\right](r^2-R_{Si}^2) \tag{19}$$

$$\phi_{Core,n}(r,z)=\phi_{0,n}(z)+\left[\left(\frac{\phi_{0,n}(z)-\phi_{s,n}(z)}{\ln(R_{Si}^2/R_{Core}^2)}\right)\left(\frac{1}{R_{Si}^2}-\frac{1}{R_{Core}^2}\right)\right]r^2 \tag{20}$$

Poisson's equations (5) and (6) are solved simultaneously at $r=R_{Core}$ to obtain relation between $\phi_{0,n}(z)$ and $\phi_{s,n}(z)$:

$$\phi_{s,n}(z)=\phi_{0,n}(z)+\frac{q\left[(N_D-N_C)+n_{i,Core}\exp\left(\phi_{i,n}(z)-V_f(z)/V_T\right)\right]R_{Core}^2\ln\left(R_{Si}/R_{Core}\right)}{2\varepsilon_{Si}} \tag{21}$$

Using (19)-(21) in equation (6) at r=0 gives 1-D differential equation in $\phi_{n,2}(z)$.

Using simulation, it was observed that the exponential term on the right hand side of (21) was very small as compared to the other term for all parameter values. Therefore, it can be neglected in this case to obtain the simplified 1-D differential equation in $\phi_{n,2}(z)$:

$$\frac{d^2\phi_{0,n}(z)}{dz^2}=\frac{-q}{\varepsilon_{si}}\left(N_D-\frac{R_{Core}^2}{R_{Si}^2}\left(N_D-N_C\right)\right)=\frac{-qN_0}{\varepsilon_{si}} \tag{22}$$

where $N_0=N_D-(N_D-N_C)R^2_{Core}/R^2_{Si}$ is termed as equivalent doping which denotes the doping concentration along r=0 and is another key indicator which can be used for primary verification of the derived model.

The general solution of equation (22) in regions 1 and 3 repectively are given as [18]:

$$\phi_{0,1}(z)=V_S-E_S(z+L_{Sext})-(qN_0/2\varepsilon_{Si})(z+L_{Sext})^2 \tag{23}$$

$$\phi_{0,3}(z)=V_D-E_D(z-L_g-L_{Dext})-(qN_0/2\varepsilon_{Si})(z-L_g-L_{Dext})^2 \tag{24}$$

Here, V_S and E_S are potential and electric field at z= -L_{Sext} and V_D and E_D are potential and electric field at z= L_g + L_{Dext}.

2.3.5 Boundary Conditions in axial direction

The final expressions of central potential are obtained from (18), (23) and (24) by applying the following boundary conditions in the z-direction [18] and obtaining values of coefficients A_1, A_2, V_S, E_S, V_D, E_D, L_{Sext} and L_{Dext}.

1. Potential at the end of the lateral extensions on source and drain side respectively are given as:

   $\phi_{0,1}(-L_{Sext})=V_{bi}$ $\qquad$ $\phi_{0,3}(L_{Dext}+L_g)=V_{bi}+V_{ds}$ (25)

Here, V_{ds} is the drain bias and V_{bi} is the effective built-in voltage [18]. The value of V_{bi} as used in [18] was used in this case due to the negligible difference observed in the value of V_{bi} for shell-doped double gate and cylindrical structure using simulation.

2. Due to constant V_{bi}, the electric field at the end of the source and drain extensions is 0.

$$\left.\frac{\partial \phi_{0,1}(z)}{\partial z}\right|_{z=-L_{Sext}} = 0 \qquad \left.\frac{\partial \phi_{0,3}(z)}{\partial z}\right|_{z=L_{Dext}+L_g} = 0 \tag{26}$$

3. Continuity of potential and lateral electric field at the gate edges.

$$\phi_{0,1}(0) = \phi_{0,2}(0) \qquad \phi_{0,2}(L_g) = \phi_{0,3}(L_g)$$

$$\left.\frac{\partial \phi_{0,1}(z)}{\partial z}\right|_{z=0} = \left.\frac{\partial \phi_{0,2}(z)}{\partial z}\right|_{z=0} \qquad \left.\frac{\partial \phi_{0,2}(z)}{\partial z}\right|_{z=Lg} = \left.\frac{\partial \phi_{0,3}(z)}{\partial z}\right|_{z=Lg} \tag{27}$$

Applying appropriate boundary conditions from (25)-(27), the final expressions of central potentials in region 1, 2 and 3 are given as:

$$\phi_{0,1}(x) = V_{bi} - k_1(z + L_{Sext})^2 \qquad -L_{Sext} \le x \le 0 \tag{28}$$

$$\phi_{0,2}(z) = \frac{B_1 \sinh(z/\lambda) + B_2 \sinh((L_g - z)/\lambda)}{\sinh(L_g/\lambda)} + V_L \qquad 0 \le x \le L_g \tag{29}$$

$$\phi_{0,3}(x) = V_{bi} + V_{ds} - k_1(z - L_g - L_{Dext})^2 \qquad L_g \le x \le L_g + L_{Dext} \tag{30}$$

Here, $B_1 = V_{bi} + V_{ds} - V_L - k_1 L_{Dext}^2$

$B_2 = V_{bi} - V_L - k_1 L_{Sext}^2$ $\quad k_1 = \frac{qN_0}{2\varepsilon_{si}}$ $\quad k_2 = \frac{qN_0\lambda}{\varepsilon_{si}}$

The value of lateral extensions L_{Sext} and L_{Dext} can be obtained from the following equations:

$$c_1 L_{Sext}^2 + c_2 L_{Sext} + c_3 = (c_4 L_{Sext}^2 + c_5 L_{Sext} + c_6)^2 \tag{31}$$

$$c_1 L_{Dext}^2 + c_2 L_{Dext} + c_7 = (c_4 L_{Dext}^2 + c_5 L_{Dext} + c_8)^2 \tag{32}$$

where

$$c_1 = k_2^2 \cosh\left(L_g/\lambda\right) \quad c_2 = 2k_2^2\lambda \sinh\left(L_g/\lambda\right) \quad c_3 = 2k_2\lambda\left(V_{ds} - \left(V_{bi} - V_L\right)\left(\cosh\left(L_g/\lambda\right) - 1\right)\right)$$

$$c_4 = -k_1 \sinh\left(L_g/\lambda\right) \quad c_5 = -k_2 \cosh\left(L_g/\lambda\right) \quad c_6 = \left(V_{bi} - V_L\right)\sinh\left(L_g/\lambda\right)$$

$$c_7 = -2k_2\lambda\left(V_{ds}\cosh\left(L_g/\lambda\right) + \left(V_{bi} - V_L\right)\left(\cosh\left(L_g/\lambda\right) - 1\right)\right) \quad c_8 = \left(V_{bi} + V_{ds} - V_L\right)\sinh\left(L_g/\lambda\right)$$

Chapter 3

RESULTS AND PRELIMINARY ANALYSIS

3.1 Key indicators

The natural length (λ), long channel potential (V_L) and equivalent doping term (N_0) obtained in equations in (17) and (22) can act as key indicators for preliminary validation of the derived analytical model. The model should satisfy the following conditions to be valid, as the derived model did for the case of shell-doped double gate JL MOSFET [18]:

1. The natural length obtained for the shell-doped CNW JL MOSFET should be identical to that obtained in the CNW JL MOSFET with uniform doping [22].
2. The long channel potential obtained for the shell-doped CNW JL MOSFET should be same as the potential obtained for a long channel device by solving the 1D Poisson's equation along the radial direction.
3. The equivalent doping concentration (N_0) should not be less than core doping concentration (N_C) and should not be more than shell doping concentration (N_D).

3.2 Parabolic Approximation Function

When the analytical model was derived using the parabolic approximation method, the following information was obtained from the key indicators:

1. Natural length (λ) is identical to those obtained for CNW JL with uniform doping (conventional case) [22],

$$\lambda = \sqrt{\frac{R_{Si}\left(2+gR_{Si}\right)}{4g}} \qquad \text{where} \qquad g = \frac{\varepsilon_{ox}}{\varepsilon_{Si} R_{Si} \ln\left(1+T_{ox}/R_{Si}\right)}$$

2. Derived long channel potential (V_L) did not match with the long channel potential obtained using 1D Poisson's equation along radial direction.

Expected V_L: $$V_L = V_{gs} - V_{fb} + \frac{qN_D\lambda^2}{\varepsilon_{si}} - \frac{q\left(N_D - N_C\right)R_{Core}^2}{\varepsilon_{si}}\left(\frac{\lambda^2}{R_{Si}^2} + \frac{1}{2}\ln\left(\frac{R_{Si}}{R_{Core}}\right)\right)$$

Obtained V_L: $V_L = V_{gs}^{'} + \frac{q\lambda^2}{\varepsilon_{si}}\left[2N_D - N_C - \frac{R_{Core}}{R_{Si}}\left(N_D - N_C\right)\right] + \frac{q\left(N_D - N_C\right)R_{Core}\left(R_{Core} - R_{Si}\right)}{2\varepsilon_{si}}$

3. Equivalent doping at r = 0 (N_0), which should have the value between core doping (N_C) and shell doping (N_D) was found to be much greater than the shell doping for some values of R_{Core}.

$$N_0 = 2N_D - N_C - \frac{R_{Core}}{R_{Si}}\left(N_D - N_C\right)$$

These observations indicated that the derived model showed severe violation of physical phenomenon associated with the device. Thus, the parabolic approximation method failed to provide an analytical model for shell-doped CNW JL MOSFET.

3.3 New Approximation Function

With the new potential approximation function, the value of the key indicators was obtained as follows:

1. Natural length (λ) is identical to those obtained for CNW JL with uniform doping (conventional case) [22],

$$\lambda = \sqrt{\frac{R_{Si}\left(2 + gR_{Si}\right)}{4g}} \qquad \text{where} \qquad g = \frac{\varepsilon_{ox}}{\varepsilon_{Si} R_{Si} \ln\left(1 + T_{ox}/R_{Si}\right)}$$

2. The long channel potential (V_L) obtained from the derived model matched with the long channel potential obtained using 1D Poisson's equation along radial direction.

$$V_L = V_{gs} - V_{fb} + \frac{qN_D\lambda^2}{\varepsilon_{si}} - \frac{q\left(N_D - N_C\right)R_{Core}^2}{\varepsilon_{si}}\left(\frac{\lambda^2}{R_{Si}^2} + \frac{1}{2}\ln\left(\frac{R_{Si}}{R_{Core}}\right)\right)$$

3. The equivalent doping (N_0) concentration lied between the permissible range of core doping and shell doping for all cases.

$$N_0 = N_D - \frac{R_{Core}^2}{R_{Si}^2}\left(N_D - N_C\right)$$

3.4 Validity of New Function over Parabolic Function

Figure 3.1 shows the plot of long channel potential for different values of R_{Core} for the models derived using parabolic approximation function and new approximation function. The figure also shows the long channel potential obtained from 1D Poisson's equation. It is observed that the V_L obtained from new approximation function is identical to the expected value of V_L for all values of R_{Core} while the V_L obtained from the parabolic approximation function shows deviation from the expected value and this deviation increases drastically for smaller values of R_{Core}.

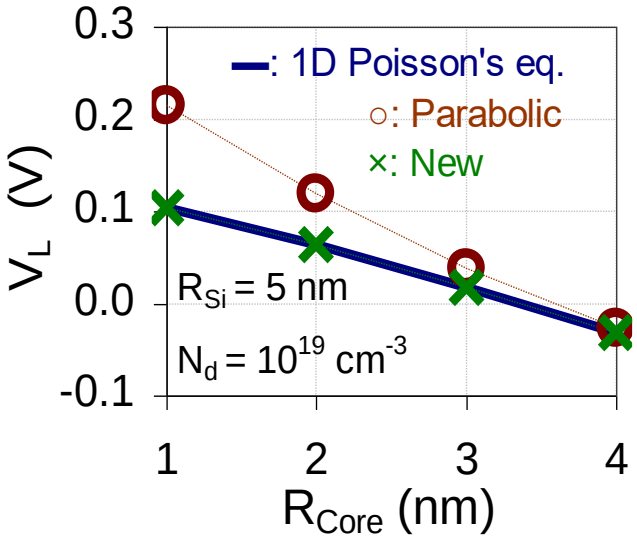

Figure 3.1 Long channel potential (V_L) for different values of R_{Core} for derived models

Figure 3.2 shows the plot of ratio of equivalent doping concentration (N_0) and shell doping concentration (N_d) for different values of R_{Core} for the models derived using parabolic approximation function and new approximation function. As N_0 cannot be greater than N_d, the maximum permissible value of this ratio is 1. It is observed that N_0 obtained using parabolic approximation function does not satisfy this condition for smaller values of R_{Core} while the ratio obtained from model derived using new approximation function never exceeds the maximum limit of 1.

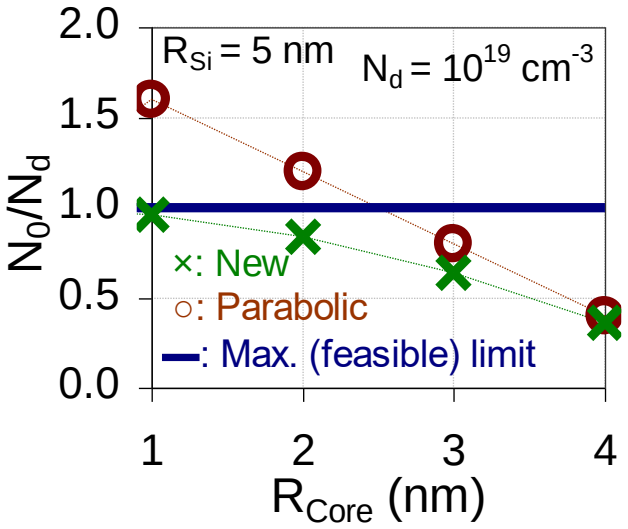

Figure 3.2 Ratio of equivalent doping (N_0) and shell doping (N_d) for different values of R_{Core} for derived models

3.5 Modeled Results

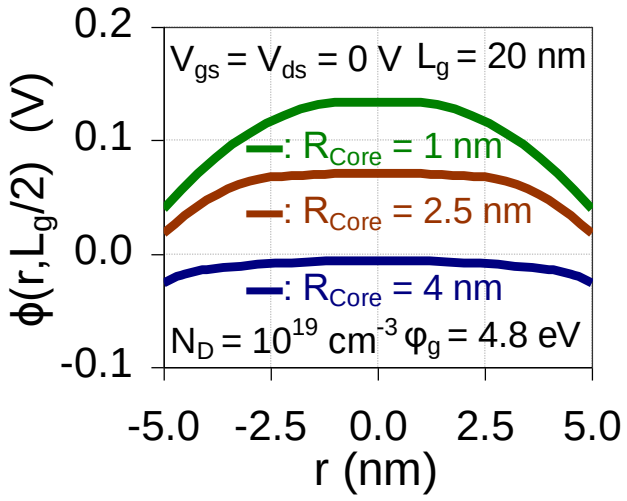

Figure 3.3 Variation of potential along radial direction at z=L_g/2 for different values of R_{Core}

Figure 3.3 shows the variation of the potential along radial direction at z=L_g/2 and figure 3.4 shows the variation of central potential ($\phi_0(z)$) along axial direction for different values of R_{Core}. It is observed that the value of potential decreases as R_{Core} increases. This is because for a fixed value of device radius R_{Si}, the shell thickness (R_{Si}-R_{Core}) decreases with increase in R_{Core}.This

reduces the number of dopants available for screening of gate electric field, which increases its influence on the channel.

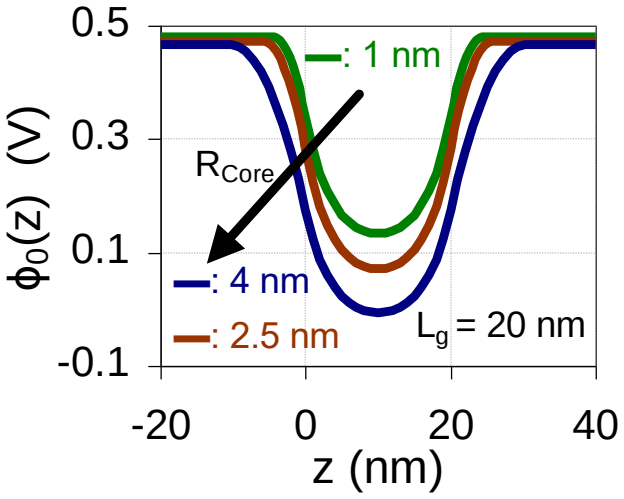

Figure 3.4 Variation of central potential ($\phi_0(z)$) along axial direction for different values of R_{Core}

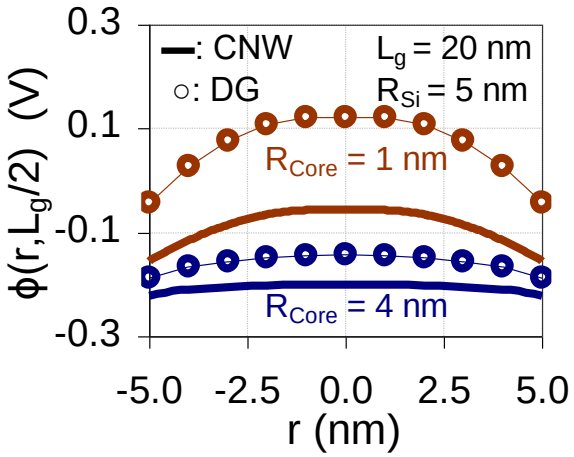

Figure 3.5 Comparison of channel potential of shell-doped DG JL MOSFET [18] and developed shell-doped CNW JL MOSFET. For DG JL MOSFET, Tsi = 2Rsi and Tcore =2Rcore. Other device parameters are identical as taken in Fig. 3 of ref. [18]

Figure 3.5 shows the comparison of the potential of the double gate (DG) and cylindrical nanowire (CNW) topology of the shell-doped junctionless MOSFET. It is observed that the value

of the potential for CNW case is less than that for DG case for all values of r. This is because CNW has a gate-all-around structure and therefore, the influence of gate electric field on the channel is more in this case. This leads to reduced channel potential in the case of CNW as compared to the DG structure.

Chapter 4

CONCLUSION AND SCOPE FOR FUTURE WORK

4.1 Conclusion

Newer devices and topologies are continuously being introduced in the semiconductor industry to carry on with the process of downscaling of transistors and fitting more and more transistors on a single chip. One such recent addition in this list of new unconventional transistor is the shell-doped MOSFET [6],[7] which has shown the potential of overcoming the challenges faced in downscaling of existing devices like conventional MOSFETs and JFETs. Therefore, to understand the physical properties of the device and optimize the device for various subthreshold applications, we developed an analytical model for shell-doped Cylindrical Nanowire Junctionless MOSFET.

The existing methods for model development were analyzed. However, the model derived using the well-established Parabolic Approximation Method failed to give a physically acceptable model for the device. The natural length (λ), long channel potential (V_L) and equivalent doping term (N_0) acted as crucial key indicators which proved the invalidity of the model. The uniqueness of this work lies in using a new potential approximation function, which was used to derive the analytical model for CNW JL MOSFET. The derived model passed all the preliminary tests of validation and gave physically acceptable results as shown in chapter 3.

The developed analytical model gives the potential expressions in the subthreshold regime throughout the device. This channel potential can be used to estimate and optimize the short channel effects (SCEs) like DIBL, subthreshold swing and subthreshold leakage current in the device.

4.2 Scope for Future Work

To keep up with the pace of the Moore's law scaling projections [8], [9], newer structures and devices will continue to emerge in the semiconductor industry. In order to exploit the properties

of these new devices, development of analytical models is necessary. In this project, a new potential approximation function is introduced which successfully gave the analytical model for CNW JL MOSFET. In the future, the application of this new approximation function can be extended to develop analytical models for other devices.

References

[1] B. G. Streetman, and S. K. Banerjee, Solid State Electronic Devices, 6th Edition, PHI Learning Private Limited, India, 2008

[2] M. T. Bohr and I. A. Young, “CMOS scaling trends and beyond,” IEEE Micro, vol. 37, no. 6, pp. 20-29, 2017.

[3] J.-P. Colinge, “Multi-gate SOI MOSFETs,” Microelectronics Engineering, vol. 84, no. 9-10, pp. 2071-2076, 2007.

[4] C. W. Lee, A. N. Nazarov, I. Ferain, N. D. Akhavan, R. Yan, P. Razavi, R. Yu, R. T. Doria, and J.-P.Colinge, "Low subthreshold slope in junctionless multigate transistors," Applied Physics Lett., vol. 96, no. 10, p. 102106, 2010.

[5] J.-P. Colinge, C.-W. Lee, A. Afzalian, N. D. Akhavan, R. Yan, I. Ferain, P. Razavi, B. O'Neill, A. Blake, M. White, A.-M. Kelleher, B. McCarthy and R. Murphy, “Nanowire transistors without junctions,” Nature Nanotechnology, vol. 5, no. 3, pp. 225-229, 2010.

[6] Y.-J. Lee, T.-C.Cho, P.-J.Sung, K.-H.Kao, F.-K.Hsueh, F.-J.Hou, P.-C.Chen, H.-C.Chen, C.-T.Wu, S.-H.Hsu, Y.-J.Chen, Y.-M.Huang, Y.-F.Hou, W.-H.Huang , C.-C. Yang, B.-Y.Chen, K.-L.Lin, M.-C.Chen, C.-H.Shen, G.-W.Huang, K.-P. Huang, M. I. Current, Y. Li, S. Samukawa8 , W.-F. Wu, J.-M.Shieh, T.-S.Chao and W.-K.Yeh, “High performance poly Si junctionless transistors with sub-5nm conformally doped layers by molecular monolayer doping and microwave incorporating CO2 laser annealing for 3D stacked ICs applications,” IEEE International Electron Devices Meeting (IEDM), pp. 6.2.1-6.2.4, 2015

[7] Y.-J. Lee, T. C. Cho, K. H. Kao, P.-J. Sung, F. K. Hsueh, P. C. Huang, C. T. Wu, S. H. Hsu, W. H. Huang, H. C. Chen, Y. Li, M. I. Current, B. Hengstebeck, J. Marino, T. Büyüklimanli, J.-M. Shieh, T.-S.Chao, W.-F.Wu and W.-K.Yeh, “A novel junctionless FinFET structure with sub-5nm shell doping profile by molecular monolayer doping and microwave annealing,” IEEE International Electron Devices Meeting(IEDM), pp. 32.7.1-32.7.4, 2014

[8] M. P. V. Kumar, C. Y.Hu, K. H. Kao, Y. J. Lee and T. S. Chao, “Impacts of the shell

doping profile on the electrical characteristics of junctionless FETs," IEEE Trans. Electron Devices, vol. 62, no. 11, pp. 3541-3546, 2015.

[9] A. Gnudi, S. Reggiani, E. Gnani and G. Baccarani, "Analysis of threshold voltage variability due to random dopant fluctuations in junctionless FETs," IEEE Electron Device Lett., vol. 33, no. 3, pp. 336-338, 2012.

[10] S. Sahay and M. J. Kumar, "Insight into lateral band-to-band-tunneling in nanowire junctionless FETs," IEEE Trans. Electron Devices, vol. 63, no.10, pp. 4138-4142, 2016.

[11] D. Neaman, D.Biswas, Semiconductor Physics and Devices, 4th Edition, McGraw Hill Education, 2017.

[12] K. Suzuki, T. Tanaka, Y. Tosaka, H. Horie, and Y. Arimoto, "Scaling theory for double-gate SOI MOSFET's," IEEE Trans. Electron Devices, vol. 40, no. 12, pp. 2326-2329, 1993.

[13] C. P. Auth and J. D. Plummer, "Scaling theory for cylindrical, fully-depleted, surrounding-gate MOSFETs," IEEE Electron Device Lett., vol. 18, no. 2, pp. 74-76, 1997.

[14] C. Li, Y. Zhuang, S. Di, and R. Han, "Subthreshold behavior models for nanoscale short-channel junctionless cylindrical surrounding-gate MOSFETs," IEEE Trans. Electron Devices, vol. 60, no. 11, pp. 3655-3662, 2013.

[15] Q. Chen, E. M. Harrell, and J. D. Meindl, "A physical short-channel threshold voltage model for undoped symmetric double-gate MOSFETs," IEEE Trans. Electron Devices, vol. 50, no. 7, pp. 1631-1637, 2003.

[16] A.Gnudi, S. Reggiani, E. Gnani, and G. Baccarani, "Semianalytical model of the subthreshold current in short-channel junctionless symmetric double-gate field-effect transistors," IEEE Trans. Electron Devices, vol. 60, no. 4, pp. 1342-1348, 2013.

[17] X., Ying, B. Zhang, H. Lou, L. Zhang, and X. Lin, "A compact model of subthreshold current with source/ drain depletion effect for the short-channel junctionless cylindrical surrounding-gate MOSFETs," IEEE Trans. Electron Devices, vol. 63, no. 5, pp. 2176-2181, 2016.

[18] N. Jaiswal, and A. Kranti, "Modeling Short-Channel Effects in Core-Shell Junctionless MOSFET," IEEE Trans. Electron Devices, vol. 66, no. 1, pp. 292-299,

2019, doi: 10.1109/TED.2018.2881006.

[19] A. Gnudi, S. Reggiani, E. Gnani, and G. Baccarani, “Semianalytical model of the subthreshold current in short-channel junctionless symmetric double-gate field-effect transistors,” IEEE Trans.Electron Devices, vol. 60, no. 4, pp. 1342–1348, Apr. 2013, doi:10.1109/TED.2013.2247765

[20] C. Li, Y. Zhuang, S. Di and R. Han, “Subthreshold behavior models for nanoscale short-channel junctionless cylindrical surrounding-gate MOSFETs,” IEEE Trans. Electron Devices, vol. 60, no. 11, pp. 3655-3662, 2013, doi: 10.1109/TED.2013.2281395

[21] G. Hu, P. Xiang, Z. Ding, R. Liu, L. Wang, and T.-A. Tang, “Analytical models for electric potential, threshold voltage, and subthreshold swing of junctionless surrounding-gate transistors,” IEEE Trans. Electron Devices, vol. 61, no. 3, pp. 688-695, 2014, doi: 10.1109/TED.2013.2297378.

[22] T. K. Chiang, “A new quasi-2-D threshold voltage model for short-channel junctionless cylindrical surrounding gate (JLCSG) MOSFETs,” IEEE Trans. Electron Devices, vol. 59, no. 11, pp. 3127-3129, 2012, doi: 10.1109/TED.2012.2212904.

[23] Y. Xiao, B. Zhang, H. Lou, L. Zhang, and X. Lin, “A compact model of subthreshold current with source/drain depletion effect for the short-channel junctionless cylindrical surrounding-gate MOSFETs,” IEEE Trans. Electron Devices, vol. 63, no. 5, pp. 2176-2181, 2016, doi: 10.1109/TED.2016.2535247.